arXiv:2004.10385v2 [cond-mat.mes-hall] 13 May 2020

Publisher link: Phys. Rev. Appl. 13, 054030 (2020)

# Electrical Contact between an Ultrathin Topological Dirac Semimetal and a Two-Dimensional Material

Liemao Cao,[1,2] Guanghui Zhou,[3] Qingyun Wu,[1] Shengyuan A. Yang,[1] Hui Ying Yang,[4] Yee Sin Ang,[1,*] and L. K. Ang[1,†]

[1] *Science, Mathematics and Technology (SMT), Singapore University of Technology and Design (SUTD), 8 Somapah Road, Singapore 487372.*

[2] *College of Physics and Electronic Engineering, Hengyang Normal University, Hengyang 421002, China*

[3] *Department of Physics, Key Laboratory for Low-Dimensional Structures and Quantum Manipulation (Ministry of Education), and Synergetic Innovation Center for Quantum Effects and Applications of Hunan, Hunan Normal University, Changsha 410081, China.*

[4] *Engineering Product Development (EPD), Singapore University of Technology and Design (SUTD), 8 Somapah Road, Singapore 487372.*

Ultrathin films of topological Dirac semimetal, $Na_3Bi$, has recently been revealed as an unusual electronic materials with field-tunable topological phases. Here we investigate the electronic and transport properties of ultrathin $Na_3Bi$ as an electrical contact to two-dimensional (2D) metal, i.e. graphene, and 2D semiconductor, i.e. $MoS_2$ and $WS_2$ monolayers. Using combined first-principle density functional theory and nonequilibrium Green's function simulation, we show that the electrical coupling between $Na_3Bi$ bilayer thin film and graphene results in a notable interlayer charge transfer, thus inducing sizable $n$-type doping in the $Na_3Bi$/graphene heterostructures. In the case of $MoS_2$ and $WS_2$ monolayers, the lateral Schottky transport barrier is significantly lower than many commonly studied bulk metals, thus unraveling $Na_3Bi$ bilayer as a high-efficiency electrical contact material for 2D semiconductors. These findings opens up an avenue of utilizing topological semimetal thin film as electrical contact to 2D materials, and further expands the family of 2D heterostructure devices into the realm of topological materials.

## I. INTRODUCTION

Two-dimensional (2D) layered materials and topological semimetals represent two of the most active research fields of current condensed matter physics, material science and applied device engineering. The ever-expanding family of 2D materials, such as graphene [1], transition metal dichalcogenides (TMDCs) [2], black phosphorus [3], group VI elemental Xenes [4], MXenes [5], and the ferromagnetic $Cr_2Ge_2Te_6$ and $Fe_3GeTe_2$ [6, 7], has been widely regarded as a key material class of key importance in electronic [8], photonic [9], optoelectronic [10], energetic [11], spintronic [12] and valleytronic [13, 14] devices with strong potential in revolutionizing the next-generation solid-state technology. Electrically contacting 2D materials with metal, however, remains one of the major bottlenecks towards the realization of high-performance industrial-grade electron devices. Although having Ohmic contact is more desirable in reducing power dissipation [15–17], most 2D semiconductors are inevitably plagued by the formation of Schottky contacts with inherently large contact resistance when contacted by a bulk metal [18–21]. Achieving high-quality electrical contact to 2D materials remains an ongoing quest critically important for the development of industrial-grade 2D-material-based devices [22, 23].

On the other hand, three-dimensional (3D) topological semimetals [24–26] which host exotic topologically protected band crossing in the bulk and topological surface states represents another emerging condensed matter system. For example, 3D topological *Dirac semimetal*, such as $Cd_3As_2$ and $Na_3Bi$ [27, 28], which hosts a pair of 3D massless Dirac quasiparticles have attracted considerable interest in the experimental and theoretical communities [29–31]. The unusual physical properties of topological semimetals has led to myriads of unusual physical properties, such as the chiral anomaly [30], linear quantum magnetoresistance [32, 33], oscillating quantum spin Hall effect [34], exceptional charge carrier mobility exceeding 6000 $cm^2V^{-1}s^{-1}$ [35], logarithmically diverging giant diamagnetism at the Dirac nodal point [36, 37], gate-tunable surface states [38], and the strong optical nonlinearity [39]. Intriguingly, $Na_3Bi$ becomes a topological insulators with a bandgap of $\sim 300$ meV in the ultrathin limit of a few atomic layers [40] in which the band structure can be tuned between topological insulator and band insulator via an external electric field [41]. The experimental demonstration of field-effect tunable topological phase transition in $Na_3Bi$ bilayer [40] thus opens up possibilities of *topological* nano-device in which the charge conduction is controlled by the field-effect modulation of the *band topology* of the transport channel.

Although both 2D materials and 3D topological semimetals have been extensively studied, the union of topological Dirac semimetals and 2D material in terms of contact engineering remains largely unknown thus far. In this work, we explore the integration of topological

* yeesin_ang@sutd.edu.sg
† ricky_ang@sutd.edu.sg

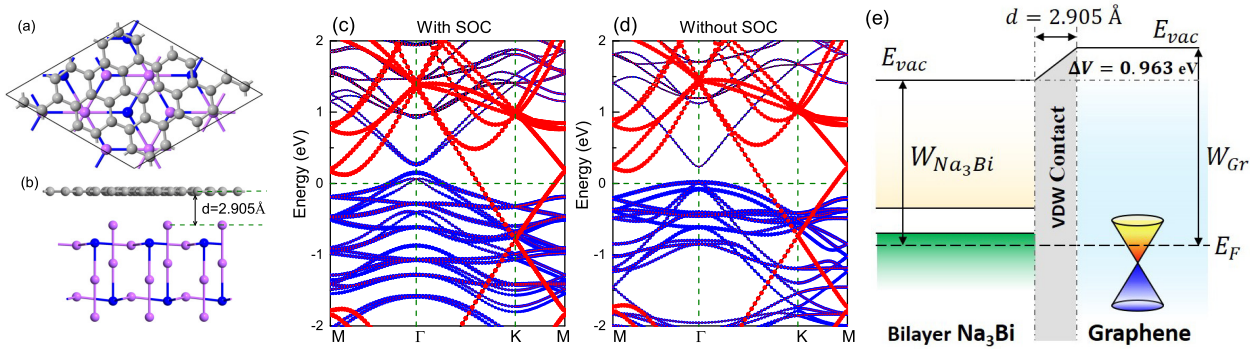



FIG. 1. (a) Top view and (b) side view of bilayer-$Na_3Bi$/graphene heterostructure. (c) and (d) Projected band structures with SOC and without SOC, respectively. The blue (red) dot projection originates from bilayer-$Na_3Bi$ (graphene). (e) Band alignments of the Graphene/$Na_3Bi$ heterostructure. $\Delta V$ represents the potential change generated by the interaction between graphene and bilayer-$Na_3Bi$. The work function of $Na_3Bi$ and graphene are denoted as $W_{Na_3Bi}$ and $W_{Gr}$, respectively.

semimetal ultrathin film into the design of 2D-material-based electronic devices. We propose a previously unexplored concept of utilizing ultrathin films of topological semimetals as aelectrical contact to 2D materials. Using a field-effect transistor setup, we show that the Schottky barrier height (SBH) formed at the bilayer-$Na_3Bi$/2D-semiconductor is markedly lower than that formed by many bulk metals (see Fig. 6 below), thus unraveling the potential of $Na_3Bi$ ultrathin film as an efficient electrode to 2D semiconductors. Furthermore, unlike many bulk metals that *metalizes* the 2D semiconductor during contact formation, the electronic band structures of $MoS_2$ and $WS_2$ remain intact when contacted by $Na_3Bi$, thus offering a useful platform for the optoelectrical studies of optics, valley and excitonic physics in 2D TMDCs [42, 43]. Importantly, ultrathin $Na_3Bi$ undergoes metal-to-insulator transition, and a topological phase transition from trivial band insulator to topological insulator with conducting edge states, when it is subjected to an external gate-voltage [40, 41]. Such gate-tunable electronic properties may be further harnessed as a functional control for designing electronic devices not found in normal metal-semiconductor contact. Our findings shall open up an avenue towards sub-10 nm device technology via the union of 2D materials and the ultrathin films of 3D topological materials, and further expands the family of 2D-material-based heterostructure devices into the realm of quantum materials with nontrivial topological phases.

## II. COMPUTATIONAL METHODS

We perform a first-principle density functional theory (DFT) simulation as implemented in the VASP code[44, 45] to study the contact between ultrathin bilayer $Na_3Bi$ with: (i) semimetallic graphene; and (ii) semiconducting $MoS_2$ and $WS_2$ monolayers. The geometric optimization and electronic properties of the heterostructures were calculated via DFT simulation as implemented in the VASP code [44, 45]. The calculation uses the projector augmented-wave (PAW) pseudopotential [46]. During the structure relaxations, the spin-orbit coupling (SOC) is not included. The SOC is included in the electronic structure calculations. The cutoff energy set to 500 eV. The vacuum layer of 30 Å in the vertical direction was chosen to avoid the surfaces interaction between the top and bottom. Monkhorst-Pack $k$-point sampling is set to be $11 \times 11 \times 1$. The method of Grimme (DFT-D3) for vdW interaction functional is adopted in the calculations [47], and the dipole correction was also added. The residual force was converged to smaller than 0.01 eV/Å, and the convergence criterion of total energy is set to be $10^{-6}$ eV. In addition, the transport properties for the two-probe systems are calculated using the Atomistix Toolkit (ATK) 2018 package based on DFT combined with the nonequilibrum Green's functions (NEGF) [48–51]. SOC is also included in the transport simulation.

## III. RESULTS AND DISCUSSIONS

### A. Bilayer-$Na_3Bi$/graphene heterostructure

Figures 1(a) and 1(b) illustrate the graphene/bilayer-$Na_3Bi$ heterostructure in top and side views, respectively. The optimized lattice parameters of bilayer $Na_3Bi$ are $a = b = 5.448$ Å, which agrees with the previously reported values [27], and that of the graphene is 2.46 Å. We consider a supercell with (2×2) and ($\sqrt{19} \times \sqrt{19}$) periodicity for $Na_3Bi$ bilayer and graphene, respectively. The lattice mismatch is 0.79 %, and we stretch the graphene system while keeping the $Na_3Bi$ lattice fixed so to preserve the electronic properties of $Na_3Bi$. The energetically most stable configuration, depicted in Fig.1(a), is obtained by optimizing the lateral displacements of the graphene along the $x$ and $y$ directions with the vertical distance between the bilayer-$Na_3Bi$ and graphene (see Fig. S1 of Supplemental Material [52]). The distance of the van der Waals (VDW) gap is 2.905 Å at equilibrium.

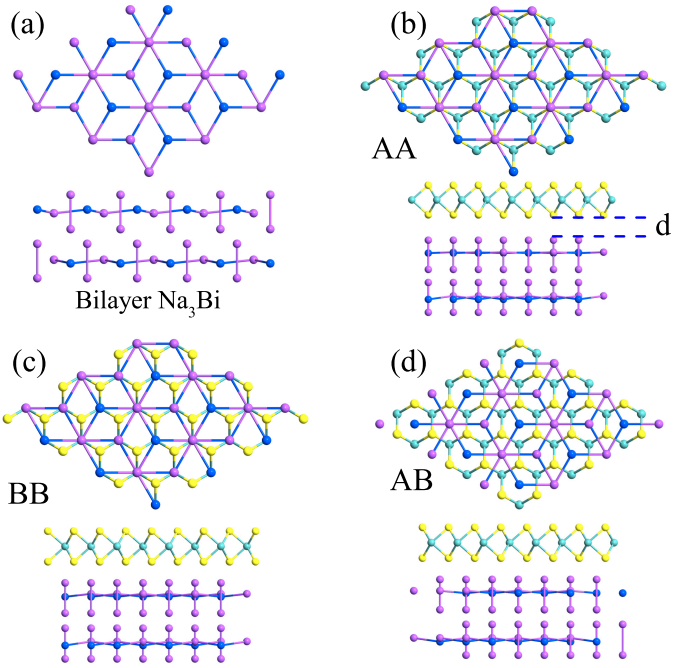



FIG. 2. (a) Optimized structural geometry of bilayer-$Na_3Bi$ in top (top panel) and side view (bottom panel). (b)-(d) Same as (a) but with different stacking configurations for $Na_3Bi/MoS_2$ and $Na_3Bi/WS_2$. $d$ is the interlayer distance.

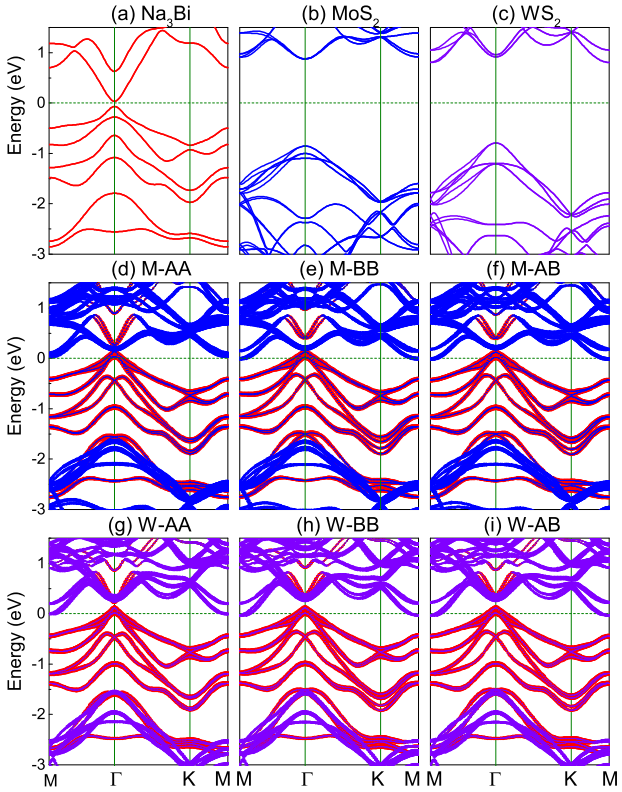



FIG. 3. The band structural of bilayer $Na_3Bi$ (a), $\sqrt{3}\times\sqrt{3}$ $MoS_2$ (b), and $\sqrt{3}\times\sqrt{3}$ $WS_2$ (c), respectively. (d)-(f) Projected band structures of the heterostructure with SOC for $Na_3Bi/MoS_2$ vdWHs by different stack. (g)-(i) Projected band structures of the heterostructure with SOC for $Na_3Bi/WS_2$ vdWHs by different stack.

The projected electronic band structure with and without SOC for the graphene/$Na_3Bi$ heterostructure shown in Fig. 1(c) and 1(d), respectively. The electronic band structures of both $Na_3Bi$ and graphene are well-preserved upon forming the heterostructure while the band gap of the bilayer $Na_3Bi$ is modified from 300 meV to 121 meV when SOC is included. Here, graphene is $n$-doped because of the larger work function of graphene that leads to the transfer of electrons from $Na_3Bi$ to graphene. Such transfer also causes some of the valence band of the $Na_3Bi$ to cross the Fermi level (see Fig. 1(e) for the band alignments of bilayer-$Na_3Bi$/graphene contact). Similar $n$-type doping has also been identified in graphene/$Cd_3As_2$ heterostructure [53], thus suggesting the $n$-doping as a common feature in graphene/ultrathin-Dirac-semimetal heterostructures. In contrast, dominantly $p$-type doping have been reported in graphene contacted by bulk metals [54–56].

### B. Bilayer-$Na_3Bi/MoS_2$ and bilayer-$Na_3Bi/WS_2$ heterostructures

We next study the contact between bilayer $Na_3Bi$ and the monolayers of $MoS_2$ and $WS_2$ (see Fig. 2). The $Na_3Bi/MoS_2$ and $Na_3Bi/WS_2$ heterostructures are constructed via stacking along the $z$-direction. For $MoS_2$ and $WS_2$, the lattice parameters are $a = b = 3.182$ Å and 3.180 Å, respectively. The $(\sqrt{3}\times\sqrt{3})$ unit cells of $MoS_2$ and $WS_2$ were adjusted to match the $(1\times1)$ unit cell of bilayer $Na_3Bi$. The lattice mismatches are 0.77% and 0.73%, respectively. In Figs. 2(b)-2(d), we show the three possible stacking modes, namely the AA, BB, and AB stacking configurations of $Na_3Bi/MoS_2$ as a representative example as the $WS_2$-based contact exhibits the same stacking structures. Here, all S (yellow) [Mo (dark cyan)] atoms are above the Na (purple) and Bi (blue)

TABLE I. Calculated parameters of the $Na_3Bi$/2D-semiconductor heterostructures. $d$ is the interlayer distance. $d_a$ is the minimum distance between Na and S atoms. $E_b$ is the binding energy. $E_{g(N)}$ and $E_{g(S)}$ are the band gap for $Na_3Bi$ and $MoS_2/WS_2$ after contact, respectively. $D$ is the dipole moment, $W$ represent the work function of the system.

| | $Na_3Bi/MoS_2$ | | | $Na_3Bi/WS_2$ | | |
|---|---|---|---|---|---|---|
| Stacking | AA | BB | AB | AA | BB | AB |
| $d$(Å) | 2.665 | 2.186 | 2.198 | 2.696 | 2.257 | 2.269 |
| $d_a$(Å) | 2.665 | 2.84 | 2.85 | 2.696 | 2.90 | 2.90 |
| $E_b$ (eV) | −3.667 | −3.831 | −3.827 | −3.543 | −3.673 | −3.668 |
| $E_{g(N)}$ (eV) | 0.131 | 0.274 | 0.278 | 0.116 | 0.279 | 0.249 |
| $E_{g(S)}$ (eV) | 1.701 | 1.653 | 1.709 | 1.558 | 1.547 | 1.522 |
| $D$ (Debye) | 1.063 | 1.091 | 1.099 | 0.873 | 0.929 | 0.919 |
| $W$ (eV) | 4.236 | 4.265 | 4.310 | 3.975 | 4.005 | 4.001 |

atoms in AA (BB) cases and all atoms of $Na_3Bi$ lie directly over the center of a hexagon in the upper $MoS_2$ (or $WS_2$) sheet in the AB cases. The total energy of the $Na_3Bi/MoS_2$ and $Na_3Bi/WS_2$ heterostructures at different values of interlayer distances is shown in Fig. S2 [52]. After structural relaxation, we find that the different stacking modes exhibit various interlayer distances (see Table 1). As the interlayer distances are close to the sum of the covalent radii of Na and S atoms, covalent bonds are expected to form between the two layers. To examine the energetic stability of $Na_3Bi/MoS_2$ and $Na_3Bi/WS_2$ electrical contacts, the binding energy $E_b$ is calculated as $E_b = E_{Na_3Bi/MoS_2(WS_2)} - E_{Na_3Bi} - E_{MoS_2(WS_2)}$, where $E_{Na_3Bi/MoS_2}$ represent the total energies of the heterostructure, $E_{Na_3Bi}$ and $E_{MoS_2(WS_2)}$ represent the energy of the isolated $Na_3Bi$ and $MoS_2$ ($WS_2$), respectively. The calculated binding energies have negative values, thus indicating that the structures considered in our simulations are energetically stable. The calculated heterostructure parameters are summarized in Table I. [see Supplemental Material for the calculated work functions, spatial electrostatic potential distributions of BB stack $Na_3Bi$-$MoS_2/WS_2$ [52]]

The band structures of an isolated bilayer $Na_3Bi$ and $\sqrt{3}\times\sqrt{3}$ $MoS_2$ ($WS_2$) monolayer are shown in Figs. 3(a)-(c). The bilayer $Na_3Bi$ exhibits a direct band gap of 0.1 eV at the Γ point which is consistent with previous results [40]. The band gap is 1.73 eV for $MoS_2$, and 1.6 eV for $WS_2$, which are slightly less than those reported in previous studies due to the presence of strain in the heterostructures considered here [57]. The projected band structures of the electrical contacts are shown in Figs. 3(d)-(i) (see Fig. S3 for the projected band structures without SOC in [52]). Here, red, blue and violet symbols denote the contributions from the $Na_3Bi$, $MoS_2$ and $WS_2$, respectively. Compared with the band structures of isolated bilayer $Na_3Bi$, $\sqrt{3}\times\sqrt{3}$ $MoS_2$ and $WS_2$ [Figs. 3(a)-(c)], the band structures of $Na_3Bi$ are not only up-shifted and show metallic behavior, but also exhibit obvious band splitting. Strong splitting of the valence band around −0.5 eV at the Γ point is observed, which originates from the interactions between $Na_3Bi$ bilayer and 2D TMDCs when forming the hereostructure. For both $MoS_2$ and $WS_2$, their valance bands are energetically down-shifted.

Interestingly, the conduction band minimum (CBM) is shifted from the Γ point to the $M$ point, and crosses the Fermi level, thus indicating the formation of an ohmic contact across the VDW gap [see Figs. 3(g)-(i)]. The ohmic contacts persists even in the case of 10-layer-$Na_3Bi$ ($\sim$ 5 nm) contacts to $MoS_2$ and $WS_2$ (see Fig. S4 in [52]). Such ohmic vertical interface is in stark contrast to the case of 2D TMDCs contacted by Au and Ag where a Schottky barrier is formed across the vertical VDW gap [58, 60, 61], which impedes the efficiency of charge injection. For other bulk metal electrodes such as Sc, Ti and Pt, the band structures of 2D TMDCs are metalized in the contact region [58, 60, 61]. This is again in contrast

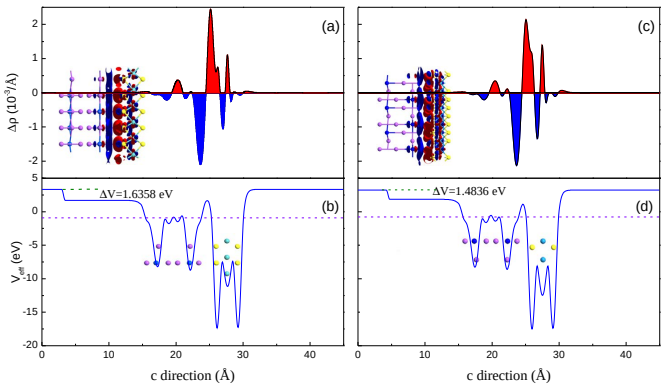



FIG. 4. Plane-averaged differential charge density $\Delta\rho$ and electrostatic potentials of the $Na_3Bi$ with (a, b) $MoS_2$; and (c, d) $WS_2$ heterostructure at the equilibrium along $z$ direction, respectively. The inset shows the side views of the isosurfaces of differential charge density of the heterostructure. The $\Delta V$ reflects the difference between the work function on the $Na_3Bi$ side and on the 2D semiconductor side.

to the case of $Na_3Bi$ contacts to 2D TMDCs where the hybridization between the two materials is weak. The band structures of 2D TMDCs are retained without the formation of Schottky barrier across the vertical contact interface. Such Ohmic nature of the $Na_3Bi$-contacted $MoS_2$ and $WS_2$ suggests that electrons can be more efficiently injected through the vertical interfaces – a favorable characteristic for electronics and optoelectronics applications.

To further understand the detailed nature of the charge transfer at the $Na_3Bi$ and $MoS_2/WS_2$ interfaces, we calculate the charge difference between the combined heterostructure system and the sum of the isolated $Na_3Bi$ and $MoS_2/WS_2$ in Figs. 4(a) and 4(c). The charge density difference is calculated as: $\Delta\rho = \rho_H - \rho_{Na_3Bi} - \rho_{MoS_2/WS_2}$, where the $\rho_H$, $\rho_{Na_3Bi}$, $\rho_{MoS_2/WS_2}$ are the charge density of the heterostructure, freestanding bilayer $Na_3Bi$, and isolated $MoS_2$ or $WS_2$, respectively. The blue regions represent electron depletion, while the red region represents the accumulation of electrons in the heterostructures relative to their two isolated components. At the interfacial region, several charge transfer oscillations are observed. The main charge depletion is contributed by the first layer of the $Na_3Bi$ closest to $MoS_2$ or $WS_2$. Moreover, some extra charge is found to be accumulating around the Mo and W atoms. Compared with metal-$MoS_2/WS_2$ contacts, the major difference is the charge accumulation located in $MoS_2$ or $WS_2$ interfaces [57, 58]. In general, both the charge depletion and the charge accumulation constitute the interface charge redistribution behavior, leading to electron wave function polarization and, hence, the formation of interfacial electric dipole. The presence of such interface dipole directly modifies the interfacial band alignment [59], thus leading to the band structures modification show in Figs. 3(d)-(i) in the main text.

To illustrate the key strengths of ultrathin $Na_3Bi$ as an

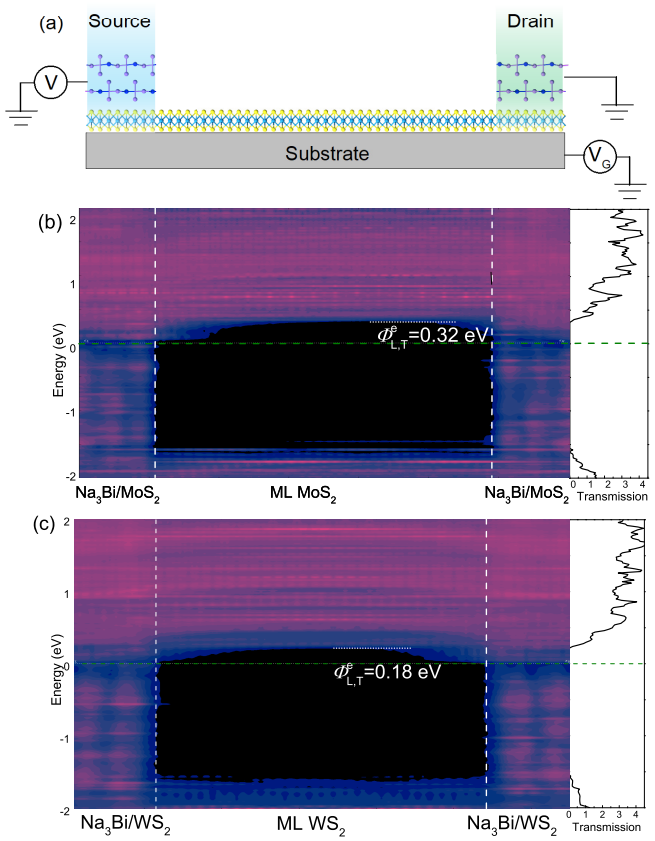



FIG. 5. (a) Schematic of a 2D TMDCs field-effect transistor. (b) and (c) LDDOS (left panels) and transmission spectra (right panels) of $MoS_2$ and $WS_2$ transistor with $Na_3Bi$ electrodes at zero gate and bias voltages. The green horizontal line represent the Fermi level.

electrical contact to 2D TMDCs over other bulk metals, we simulate a field-effect transistor device with a 5-nm channel length [see Fig. 5(a)]. We employ a nonequilibrium Green's function (NEGF) approach [52] to extract the *lateral transport Schottky barrier height* laterally extending into the 2D channel by calculating the local device density of states (LDDOS) which reflects the energy-band distribution in real-space along the simulated device [62, 63]. The lateral electron SBH ($\Phi^e_{L,T}$) of the $MoS_2$ and $WS_2$ transistors are estimated as the energy difference between the Fermi level, $E_F$, and the CBM of the 2D channel [labeled in Figs. 5(b) and (c)]. The $\Phi^e_{L,T}$ is calculated as 0.32 eV and 0.18 eV, respectively, for $MoS_2$ and $WS_2$ [Figs. 5(b) and (c)], which are appreciably lower than many other commonly studied bulk metals [60, 61] because of the low work function of $Na_3Bi$ bilayer (2.44 eV). In Fig. 6, $\Phi^e_{L,T}$ versus isolated metal work function ($W_M$) is plotted using the data for $WS_2$ and $MoS_2$ 5-nm field-effect transistor extracted from Refs. [60, 61]. Here $\Phi^e_{L,T}$ of bilayer-$Na_3Bi$ is substantially lower when compared to other bulk metals. Particularly for $WS_2$ contacted by $Na_3Bi$ bilayer, the $\Phi^e_{L,T}$ is the lowest com-

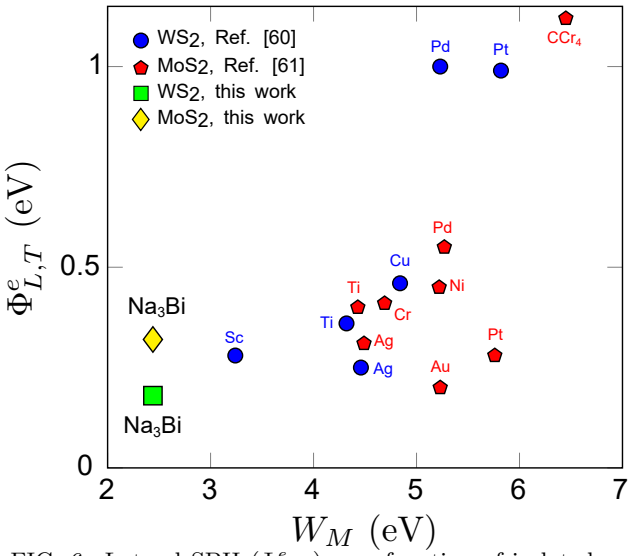



FIG. 6. Lateral SBH ($\Phi^e_{L,T}$) as a function of isolated metal work function ($W_M$) for $WS_2$ [60] and $MoS_2$ [61].

pared to other common bulk metal electrodes (i.e. Sc, Ti, Ag, Cu, Pd, and Pt) [61]. The relatively low $\Phi^e_{L,T}$ thus reveals the potential of $Na_3Bi$ bilayer as another candidate electrode material for achieving high-efficiency charge injection into 2D TMDCs. We further remark that the pronounce Stark effect in $Na_3Bi$ ultrathin film allows the band gap to be tuned and closed, and the electronic band structure to be switched between trivial band insulator and topological insulator by an external gate-voltage [40, 41]. Such gate-tunable metallic-insulator transition and topological phase transitions may offer a physical mechanism for the design of functional devices, not found in the conventional bulk-metal/semiconductor contact, that worth to be explored in future works.

Finally, we remark that $Na_3Bi$ is prone to degradation under ambient air conditions. Nonetheless, recent experiment [40] has successfully employed angle-resolved photoemission spectroscopy and scanning tunneling microscopy to study the field-effect tunable band structure in $Na_3Bi$, revealing a major step forward towards the fabrication of $Na_3Bi$ device. More recently, $Na_3Bi$ ultrathin film passivated by $MgF_2$ or Si capping layers have been demonstrated to be air-stable and the transport properties remain intact after such passivations [64]. Encapsulated $Na_3Bi$ devices thus provide a potential route towards air-stable hybrid $Na_3Bi$/2D-semiconductor devices.

## IV. CONCLUSION

In summary, we investigated the electronic and transport properties of the ultrathin topological Dirac semimetal $Na_3Bi$ as an electrical contact to graphene, $MoS_2$ and $WS_2$ via first-principle calculations. We show that the $Na_3Bi$/graphene contact leads to a $n$-type dop-

ing in graphene, which can be useful for electronics and optoelectronics applications, such as *p*-*n* junction and photodetector For $Na_3Bi/MoS_2$ and $Na_3Bi/WS_2$, the prevalence of ohmic vertical interface and low lateral Schottky barrier heights indicates the potential of $Na_3Bi$ as an energy-efficient electrical contact. The findings reported here could form the harbinger for the exploration of an emerging class of heterostructure electronic devices [65] that synergies 2D materials and the ever-expanding family of topological semimetals where nodal point, line, link, chain, double helix, hourglass, surface and many other exotic topological phases are continually being unearthed.

## ACKNOWLEDGMENTS

This project is funded by Singapore MOE Tier 2 Grant (2018-T2-1-007), A*STAR IRG Grant (IRG A1783c0011), and Hunan Provincial Natural Science Foundation of China (Grant No. 2019JJ50016), and science Foundation of Hengyang Normal University of China (No. 18D26), and the National Natural Science Foundation of China (Grant No. 11774085). All the calculations were carried out using the computational resources provided by the National Supercomputing Centre (NSCC) Singapore.

[1] A. K. Geim, and K. S. Novoselov, The rise of graphene, Nat. Mater. **6**, 183 (2007).
[2] S. Manzeli, D. Ovchinnikov, D. Pasquier, O. V. Yazyev, and A. Kis, 2D transition metal dichalcogenides, Nat. Rev. Mater. **2**, 17033 (2017).
[3] F. Xia, H. Wang, J. C. M. Hwang, A. H. Castro, and L. Yang, Black phosphorus and its isoelectronic materials, Nat. Rev. Phys. **1**, 306 (2019).
[4] A. Molle, J. Goldberger, M. Houssa, Y. Xu, S.-C. Zhang, and D. Akinwande, Buckled two-dimensional Xene sheets, Nat. Mater. **16**, 163 (2017).
[5] M. Naguib, V. N. Mochalin, M. W. Baroum, and Y. Gogotsi, 25th Anniversary Article: MXenes: A New Family of Two-Dimensional Materials, Adv. Mater. **26**, 992 (2014).
[6] C. Gong et al, Discovery of intrinsic ferromagnetism in two-dimensional van der Waals crystals, Nature **546**, 265 (2017).
[7] Y. Deng et al, Gate-tunable room-temperature ferromagnetism in two-dimensional $Fe_3GeTe_2$, Nature **563**, 94 (2018).
[8] G. Fiori, F. Bonaccorso, G. Iannaccone, T. Palacios, D. Neumaier, A. Seabaugh, S. K. Banerjee, and L. Colombo, Electronics based on two-dimensional materials, Nat. Nanotechnol. **9**, 768 (2014).
[9] F. Xia, H. Wang, D. Xiao, M. Dubey, and A. Ramasubramaniam, Two-dimensional material nanophotonics, Nat. Photon. **8**, 899 (2014).
[10] Q. H. Wang, K. Kalantar-Zadeh, A. Kis, J. N. Coleman, and M. S. Strano, Electronics and optoelectronics of two-dimensional transition metal dichalcogenides, Nat. Nanotechnol. **7**, 699 (2012).
[11] E. Pomerantseva, and Y. Gogotsi, Two-dimensional heterostructures for energy storage, Nat. Energy **2**, 17089 (2017).
[12] S. Roche et al, Graphene spintronics: the European Flagship perspective, 2D Mater. **2**, 030202 (2015).
[13] J. R. Schaibley, H. Yu, G. Clark, P. Rivera, J. S. Ross, K. L. Seyler, W. Yao, and X. Xu, Valleytronics in 2D materials, Nat. Rev. Mater. **1**, 16055 (2016).
[14] Y. S. Ang, S. A. Yang, C. Zhang, Z. Ma and L. K. Ang, Valleytronics in merging Dirac cones: All-electric-controlled valley filter, valve, and universal reversible logic gate, Phys. Rev. B **96**, 245410 (2017).
[15] A. Allain, J. H. Kang, K. Banerjee, and A. Kis, Electrical contacts to two-dimensional semiconductors, Nat. Mater. **14**, 1195 (2015).
[16] I. Popov, G. Seifeit, and D. Tománek, Designing electrical contacts to $MoS_2$ monolayer: A computational study, Phys. Rev. Lett. **108**, 156802 (2012).
[17] X. Cui, G.-H. Lee, Y. D. Kim, G. Arefe, P. Y. Huang, C.-H. Lee, D. A. Chenet, X. Zhang, L. Wang, F. Ye, F. Pizzocchero, B. S. Jessen, K. Watanabe, T. Taniguchi, D. A. Muller, T. Low, P. Kim, and J. Hone, Multi-terminal transport measurements of $MoS_2$ using a van der Waals heterostructure device platform, Nat. Nanotechnol. **10**, 534 (2015).
[18] J. H. Kang, W. Liu, D. Sarkar, D. Jena, and K. Banerjee, Computational study of metal contacts to monolayer transistion-metal dichalcogenide semiconductors, Phys. Rev. X **4**, 031005 (2014).
[19] Y. S. Ang, H. Y. Yang, and L. K. Ang, Universal Scaling Laws in Schottky Heterostructures Based on Two-Dimensional Materials, Phys. Rev. Lett. **121**, 056802 (2018).
[20] Y. S. Ang, Y. Chen, C. Tan and L. K. Ang, Generalized High-Energy Thermionic Electron Injection at Graphene Interface, Phys. Rev. Appl. **12**, 014057 (2019).
[21] Q. Y. Wu, Y. S. Ang, L. M. Cao, and L. K. Ang, Design of metal contacts for monolayer $Fe_3GeTe_2$ based devices, Appl. Phys. Lett. **115**, 083105 (2019).
[22] N. Briggs et al, A roadmap for electronic grade 2D materials, 2D Mater. **6**, 022001 (2019).
[23] A. C. Ferrari et al, Science and technology roadmap for graphene, related two-dimensional crystals, and hybrid systems, Nanoscale **7**, 4598 (2015).
[24] Z. K. Liu, B. Zhou, Y. Zhang, Z. J. Wang, H. M. Weng, D. Prabhakaran, S. K. Mo, Z. X. Shen, Z. Fang, X. Dai, Z. Hussain, and Y. L. Chen, Discovery of a Three-Dimensional Topological Dirac Semimetal, $Na_3Bi$, Science **343**, 864 (2014).
[25] S. Borisenko, Q. Gibson, D. Evtushinsky, V. Zabolotnyy, B. Bühner, and R. J. Cava, Experimental Realization of a Three-Dimensional Dirac Semimetal, Phys. Rev. Lett. **113**, 027603 (2014).
[26] M. Neupane, S.-Y. Xu, R. Sankar, N. Alidoust, G. Bian, C. Liu, I. Belopolski, T.-R. Chang, H.-T. Jeng, H. Lin, A. Bansil, F. C. Chou, and M. Z. Hasan, Observation of a Three-Dimensional Topological Dirac Semimetal Phase

in High-Mobility $Cd_3As_2$, Nat. Commun. **5**, 3786 (2014).
[27] Z. J. Wang, Y. Sun, X. Q. Chen, C. Franchini, G. Xu, H. M. Weng, X. Dai, and Z. Fang, Dirac Semimetal and Topological Phase Transitions in $A_3Bi$ (A=Na, K, Rb), Phys. Rev. B **85**, 195320 (2012).
[28] Z. J. Wang, H. M. Weng, Q. S. Wu, X. Dai, and Z. Fang, Three-Dimensional Dirac Semimetal and Quantum Transport in $Cd_3As_2$, Phys. Rev. B **88**, 125427 (2013).
[29] S. M. Young, S. Zaheer, J. C. Y. Teo, C. L. Kane, E. J. Mele, and A. M. Rappe, Dirac Semimetal in Three Dimensions, Phys. Rev. Lett. **108**, 140405 (2012).
[30] J. Xiong, S. K. Kushwaha, T. Liang, J. W. Krizan, M. Hirschberger, W. Wang, R. J. Cava, and N. P. Ong, Evidence for the Chiral Anomaly in the Dirac Semimetal $Na_3Bi$ , Science **350**, 413 (2015).
[31] C. Zhang, E. Zhang, W. Wang, Y. Liu, Z.-G. Chen, S. Lu, S. Liang, J. Cao, X. Yuan, L. Tang, Q. Li, C. Zhou, T. Gu, Y. Wu, J. Zou, and F. Xiu, Room-Temperature Chiral Charge Pumping in Dirac Semimetals, Nat. Commun. **8**, 13741 (2017).
[32] A. A. Abrikosov, Quantum magnetoresistance, Phys. Rev. B **58**, 2788 (1998).
[33] W. Zhang, R. Yu, W. Feng, Y. Yao, H. Weng, X. Dai, Z. Fang, Topological aspect and quantum magnetoresistance of $\beta$-$Ag_2Te$, Phys. Rev. Lett. **106**, 156808 (2011).
[34] C.-X. Liu, H. J. Zhang, B. Yan, X.-L. Qi, T. Frauenheim, X. Dai, Z. Fang, S.-C. Zhang, Oscillatory crossover from two-dimensional to three-dimensional topological insulators, Phys. Rev. B **81**, 041307 (2010).
[35] J. Hellerstedt, M. T. Edmonds, N. Ramakrishnan, G. Liu, B. Weber, A. Tadich. K. M. O'Donnell, S. Adam, and M. S. Fuhrer, Electronic Properties of High-Quality Epitaxial Topological Dirac Semimetal Thin Films, Nano Lett. **16**, 3210 (2016).
[36] P. Goswami, S. Chakravarty, Quantum criticality between topological and band insulators in 3+1 dimensions, Phys. Rev. Lett. **107**, 196803 (2011).
[37] M. Koshino, T. Ando, Anomalous orbital magnetism in Dirac-electron systems: Role of pseudospin paramagnetism, Phys. Rev. B **81**, 195431 (2010).
[38] X. Xiao, S. A. Yang, Z. Liu, H. Li, and G. Zhou, Anisotropic Quantum Confinement Effect and Electric Control of Surface States in Dirac Semimetal Nanostructures, Sci. Rep. **5**, 7898 (2015).
[39] K. J. A. Ooi, Y. S. Ang, Q. Zhai, D. T. H. Tan, L. K. Ang, and C. K. Ong, Nonlinear plasmonics of three-dimensional Dirac semimetals, APL Photon. **4**, 034402 (2019).
[40] J. L. Collins, A. Tadich, W. K. Wu, L. C. Gomes, J. N. B. Rodrigues, C. Liu, J. Hellerstedt, H. Ryu, S. J. Tang, S. K. Mo, S. Adam, S. A. Yang, M. S. Fuhrer and M. T. Edmonds, Electric-field-tuned topological phase transition in ultrathin $Na_3Bi$, Nature **564**, 390 (2018).
[41] H. Pan, M. Wu, Y. Liu, and S. A. Yang, Electric control of topological phase transitions in Dirac semimetal thin films, Sci. Rep. **5**, 14639 (2015).
[42] M. Eginligil, B. Cao, Z. Wang, X. Shen, C. Cong, J. Shang, C. Soci, and T. Yu, Dichroic spin-valley photocurrent in monolayer molybdenum disulphide, Nat. Commun. **6**, 7636 (2015).
[43] J. Lee, K. F. Mak, and J. Shan, Electrical control of the valley Hall effect in bilayer MoS2 transistors, Nat. Nanotechnol. **11**, 421 (2016)
[44] G. Kresse and J. Furthmüller, Efficient iterative schemes for ab initio total-energy calculations using a plane-wave basis set, Phys. Rev. B **54**, 11169 (1996).
[45] G. Kresse and J. Furthmüller, Efficiency of ab-initio total energy calculations for metals and semiconductors using a plane-wave basis set, Comput. Mater. Sci. **6**, 15 (1996).
[46] G. Kresse and D. Joubert, From ultrasoft pseudopotentials to the projector augmented-wave method, Phys. Rev. B **59**, 1758 (1999).
[47] S. Grimme, J. Antony, S. Ehrlich and H. Krieg, A consistent and accurate ab initio parametrization of density functional dispersion correction (DFT-D) for the 94 elements H-Pu, J. Chem. Phys. **132**, 154104 (2010).
[48] J. M. Soler, E. Artacho, J. D. Gale, A. García, J. Junquera, P. Ordej ón, and D. Sáchez-Portal, The SIESTA method for ab initio order-N materials simulation, J. Phys. Condens. Matter **14**, 2745 (2002).
[49] M. Brandbyge, J. L. Mozos, P. Ordejón, J. Taylor, and K. Stokbro, Density-functional method for nonequilibrium electron transport, Phys. Rev. B **65**, 165401 (2002).
[50] J. Taylor, H. Guo, and J. Wang, Ab initio modeling of quantum transport properties of molecular electronic devices, Phys. Rev. B **63**, 245407 (2001).
[51] J. Taylor, H. Guo, and J. Wang, Ab initio modeling of open systems: Charge transfer, electron conduction, and molecular switching of a C60 device, Phys. Rev. B **63**, 121104 (2001).
[52] See Supplemental Material for the total energies of bilayer-$Na_3Bi$/graphene (Fig. S1), bilayer-$Na_3Bi/MoS_2$ and bilayer-$Na_3Bi/MoS_2$ (Fig. S2), the projected band structures of bilayer-$Na_3Bi/MoS_2$ and bilayer-$Na_3Bi/MoS_2$ without SOC (Fig. S3), the 10-layer-$Na_3Bi/MoS_2$ and 10-layer-$Na_3Bi/MoS_2$ projected band structures with SOC (Fig. S4).
[53] Y.-F. Wu, L. Zhang, C.-Z. Li, Z.-S. Zhang, S. Liu, Z.-M. Liao, and D. P. Yu, Dirac Semimetal Heterostructures: 3D $Cd_3As_2$ on 2D Graphene, Adv. Mater. **30**, 1707547 (2018).
[54] G. Giovannetti, P. A. Khomyakov, G. Brocks, V. M. Karpan, J. van den Brink, and P. J. Kelly, Doping Graphene with Metal Contacts, Phys. Rev. Lett. **101**, 026803 (2008).
[55] P. A. Khomyakov, G. Giovannetti, P. C. Rusu, G. Brocks, J. van den Brink, and P. J. Kelly, First-principles study of the interaction and charge transfer between graphene and metals, Phys. Rev. B **79**, 195425 (2009).
[56] H. C. Diaz, R. Addoua, and M. Batzilla, Interface properties of CVD grown graphene transferred onto $MoS_2$(0001), Nanoscale **6**, 1071 (2014).
[57] W. Chen, E. J. G. Santos, W. G. Zhu, E. Kaxiras, and Z. Y. Zhang, Tuning the Electronic and Chemical Properties of Monolayer $MoS_2$ Adsorbed on Transition Metal Substrates, Nano Lett. **13**, 509 (2013).
[58] C. Gong, L. Colombo, R. M. Wallace, and K. Cho, The Unusual Mechanism of Partial Fermi Level Pinning at Metal-$MoS_2$ Interfaces, Nano Lett. **14**, 1714 (2014).
[59] R. T. Tung, Formation of an electric dipole at metal-semiconductor interfaces, Phys. Rev. B **64**, 205310 (2001).
[60] H. Tang, B. Shi, Y. Pan, J. Li X. Zhang, J. Yan, S. Liu, J. Yang, L. Xu, J. Yang, M. Wu, and J. Lu, Schottky Contact in Monolayer $WS_2$ Field-Effect Transistors, Adv. Theory Simul. 1900001 (2019).

[61] Y. Pan, J. Gu, H. Tang, X. Zhang, J. Li, B. Shi, J. Yang, H. Zhang, J. Yang, S. Liu, H. Hu, M. Wu, and J. Lu, Reexamination of the Schottky Barrier Heights in Monolayer $MoS_2$ Field-Effect Transistors, ACS Appl. Nano Mater. 2, 4717 (2019).

[62] S. Das, W. Zhang, M. Demarteau, A. Hoffmann, M. Dubey, and A. Roelofs, Tuanble Transport Gap in Phosphorene, Nano Lett. **14**, 5733 (2014)

[63] Y. Du, H. Liu, Y. Deng, and P. D. Ye, Device Perspective for Black Phosphorus Field-Effect Transistors: Contact Resistance, Ambipolar Behavior, and Scaling, ACS Nano **8**, 10035 (2014)

[64] C. Liu, G. Akhgar, J. L. Collins, J. Hellerstedt, S. Adam, M. S. Fuhrer, M. T. Edmonds, Quantum Transport in Air-stable $Na_3Bi$ Thin Films, arXiv:2003.13171 (2020).

[65] S.-J. Liang, B. Cheng, X. Cui, and F. Miao, Van der Waals Heterostructures for High-Performance Device Applications: Challenges and Opportunities, Adv. Mater. 1903800 (2019).